Instruments and Methods

Application of micro-X-ray fluorescence to chemical mapping of polar ice

M.C. MOREL FOURCADE,[1] J.M. BARNOLA,[1] J. SUSINI,[2] R. BAKER,[2] G. DURAND,[1] M. de ANGELIS,[1] P. DUVAL[1]

[1]*Laboratoire de Glaciologie at Géophysique de l'Environnement (CNRS–UJF), 54 rue Molière, BP 96, 38402 Saint-Martin-d'Hères Cedex, France*
E-mail: fourcade@lgge.obs.ujf-grenoble.fr
[2]*European Synchrotron Radiation Facility, 6 rue Jules Horowitz, BP 220, 38043 Grenoble Cedex, France*

ABSTRACT. Synchrotron-based micro-X-ray fluorescence (μXRF) equipment has been used to analyze impurities in polar ice. A customized sample holder has been developed and the μXRF equipment has been adapted with a thermal control system to keep samples unaltered during analyses. Artificial ice samples prepared from ultra-pure water were analyzed to investigate possible contamination and/or experimental artefacts. Analyses of polar ice from Antarctica (Dome C and Vostok) confirm this μXRF technique is non-destructive and sensitive. Experiments can be reproduced to confirm or refine results by focusing on interesting spots such as crystal grain boundaries or specific inclusions. Integration times and resolution can be adjusted to optimize sensitivity. Investigation of unstable particles is possible due to the short analysis time. In addition to identification of elements in impurities, μXRF is able to determine their speciations. The accuracy and reliability of the results confirm the potential of this technique for research in glaciology.

1. INTRODUCTION

Studying impurities in ice is essential for current research in glaciology. Issues that have to be addressed for analysis of ice cores are the fragility of the ice material, its evolving structure and the low concentrations of impurities.

Analysis of melted samples by ion chromatography gives the average ionic concentrations of soluble (mineral and organic) species, even at very low concentrations. Such information is used for studying past atmospheric composition, for example. However, due to the possible interaction between chemical impurities and physical properties it is of primary interest to know the microstructural localization of impurities. Depending on their localization, either dispersed in the ice matrix or concentrated at grain boundaries, the structure of the sample may evolve from its original in situ state. For example, reactions between soluble sulphuric acid and carbonate particulates may alter the record of atmospheric CO_2 present in air bubbles trapped in the ice (Legrand and Mayewski, 1997).

Several analytical methods have already been successfully developed to locate impurities in ice (Baker and others, 2003) or to study their effect on properties of ice (Wolff and Mulvaney, 1988; Iliescu and others, 2003). Acidic ions at a triple junction of Antarctic ice have been studied by the Raman scattering technique (Fukazawa and others, 1998). Trickett and others (2000) studied the effect of H_2SO_4 on the mechanical properties of ice by synchrotron X-ray topography. The major technique implemented to observe impurities is scanning electron microscopy with energy-dispersive X-ray microanalysis. Mulvaney and others (1988) found sulphuric acid at the grain boundaries in Antarctic ice. In the last few years, two teams have successfully developed this technique (Barnes and others, 2002, 2003; Cullen and Baker, 2002).

Whilst sublimation concentrates impurities and facilitates detection, it may also introduce artefacts: for example filaments observed in the grain boundaries of polar ice are due to the sublimation of the surrounding ice (Baker and Cullen, 2003). Developing a new experimental method that enables mapping and analysis of impurities in a non-destructive way is seen as valuable for research in glaciology. To this end we looked at the X-ray microscopy analysis technique developed at the ID21 beamline at the European Synchrotron Radiation Facility (ESRF) in Grenoble, France (Susini and others, 2002). This technique enables hydrated frozen samples to be investigated without pretreatment. It allows the study of thick samples, and, in the high-energy range produced by this technique, fluorescence yield is high enough to be mapped with significant contrast and to identify low Z elements. With these capabilities the micro-X-ray fluorescence (μXRF) technique appears a suitable basis for developing a new experimental method for mapping and analyzing impurities in a non-invasive way. In this paper, we report the technical and methodological adaptations implemented, the validation of the technique and the first results obtained.

2. EXPERIMENTAL PROCEDURE

2.1. Equipment

An analysis chamber (internal part shown in Fig. 1a) is closed by a tight door, as a high vacuum ($\sim 10^{-5}$ mbar) is necessary to lower the detection limit and to have access to low Z elements.

To preserve the ice sample from any transformation or sublimation, it must be maintained at low temperature ($\sim$120 K during analysis). The cooling system consists of a special 3 l Dewar flask ('a' in Fig. 1a), automatically filled

https://doi.org/10.3189/172756505781829340 Published online by Cambridge University Press

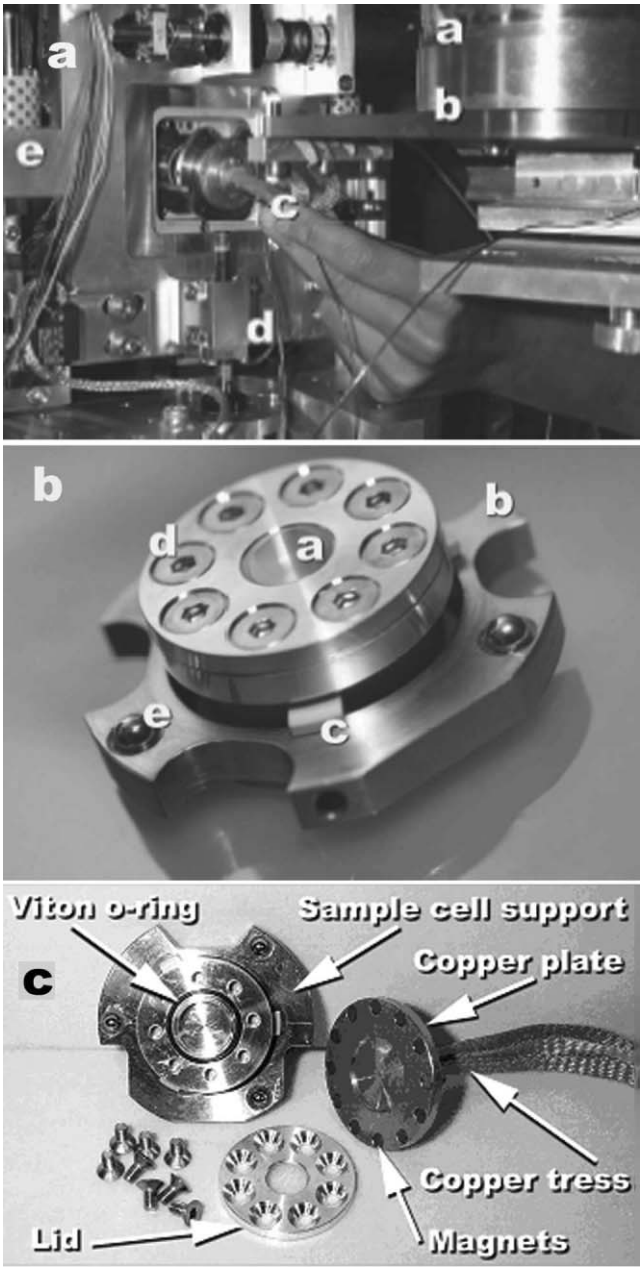

Fig. 1. (a) Internal part of the analysis chamber; a: Dewar flask; b: copper cylinder; c: copper tress; d: thermocouple; e: support of piezometer electric scanner. (b) The sample cell and its support; a: the front window; b: the sample cell support; c: Peek®; d: screw; e: magnets. (c) Details of the sample cell.

with liquid nitrogen (LN_2) and hermetically fixed to the roof of the chamber by a DN100 flange. The base of the Dewar flask is made of a thick copper cylinder ('b' in Fig. 1a) coupled to a magnetized copper plate by a flexible copper tress (Fig. 1c and 'c' in Fig. 1a), the sample cell being fixed to this plate by magnets. This maintains the temperature of the ice sample near to the same low temperature as the bottom of the Dewar flask. A thermocouple is fixed on the copper plate to measure the temperature during experiments ('d' in Fig. 1a). The upper part of Figure 1b shows the front window of the cell in which the sample is set up. The window is a transparent film of Ultralene®. Ultralene® was selected for its good X-ray transmission, its strength and purity. The film is pressed between the lid and the sample cell (Fig. 1c) with a Viton O-ring to ensure it is airtight. The sample cell is thermally isolated from its support by Peek® pieces ('c' in Fig. 1b). The sample cell and its support are made of aluminium. Magnets ('e' in Fig. 1b) fix the sample cell and the support into the piezometer-based scanner (Fig. 1a). This piezometer-based scanner moves the support of the sample cell by steps along the x and y directions. Steps are adjustable according to the lateral resolution desired. To obtain a scan rapidly, the total mass of the sample cell device associated with the piezometer has to be <100 g. Hence the choice of aluminium for the sample cell device.

2.2. Sample selection

Artificial samples

In order to estimate the contamination introduced by the sample preparation and to evaluate the background signal of the measurement procedure, one artificial ice sample (S1) was prepared from ultra-pure water.

Natural samples

Samples should be selected that provide the opportunity to evaluate the technique regarding, in particular, localization of impurities, analysis of large aggregates and speciation of elements. Two technical constraints must be dealt with: (i) the μXRF detection limit of the instrument, expected to be about 1 ppm, required samples with a significant amount of impurities; (ii) the small size of the sample cell (diameter only 11 mm) required ice with small crystals, in order to observe several grain boundaries. Accordingly, European Project for Ice Coring in Antarctica (EPICA) Dome C samples, from the Last Glacial Maximum, at 566 m depth, were selected. In addition, samples of accreted ice from Vostok lake, Antarctica at about 3570 m depth were selected to analyze aggregates.

2.3. Sample preparation

Samples were prepared at Laboratoire de Glaciologie et Géophysique de l'Environnement, Grenoble, France, in a cold room at 258 K. To prevent contamination, every tool was new and washed with methanol. Ice cores were cut into samples 7 cm long. Each sample was machined to a cylinder with the same diameter as the sample cell. The surface of each cylinder was adjusted with a microtome to exactly fit in the cell and to be flush with the cell surface on which the Ultralene® film was spread. Once the sample cell was sealed with screws, it was put into a polycarbonate box to avoid contamination of the Ultralene® film. Samples were then transferred to the ESRF at a temperature of 235 K and cooled to the temperature of LN_2 just before introduction into the analysis chamber.

2.4. Sample set up in the analysis chamber

It is critical that water vapour be prevented from entering the chamber, as this could turn into hoar on the cell window. For this reason, the chamber was put under a vacuum ($\sim 10^{-5}$ mbar). The Dewar flask was then filled with LN_2. Once the temperature of the copper plate was lowered to 113 K, the analysis chamber was brought back to atmospheric pressure with dry N_2. Outside the chamber, at the level of the top of the door, a laminar flow of dry N_2 was blown downwards to keep humidity low in the chamber at the door aperture. The door was opened, and the sample box removed from the LN_2, introduced into the chamber and opened. The sample cell and its support (Fig. 1b) were placed in the X-ray beam and fixed by magnets. The copper

https://doi.org/10.3189/172756505781829340 Published online by Cambridge University Press

plate and its tress were put in contact with the sample cell, and the door was closed. The vacuum was re-pumped and the temperature became stable at 123 K after 1.5 hours. The door was left open <1 min. The maximum temperature observed for the sample cell during set-up was 203 K. There was no hoar in the chamber except for some traces on the copper tress.

2.5. Analysis

Initially, the surface of the polar ice sample was observed using an optical microscope, in order to check the absence of hoar on the Ultralene® film, verify that the ice was intact and identify grain boundaries. Once a grain boundary or an interesting spot was selected, the ice sample was examined using the X-ray microscopy beamline ID21 (Susini and others, 2002). The X-ray beam was focused down to a microprobe of $0.5 \times 0.5\,\mu m^2$ by means of a Fresnel zone plate (Di Fabrizio and others, 1999). Two Si ⟨111⟩ crystals provided a monochromatic beam ($\Delta E/E = 10^{-4}$). The fluorescence signal was analyzed using a high energy resolution germanium solid-state detector. The incident beam energy was fixed at 4500 eV to ensure a good fluorescence yield for elements ranging from calcium to sulphur. For sulphur speciation, the excitation beam was tuned at 2482 eV. For these configurations, 4500 and 2482 eV, the probed depth (z axis) is 50 and 25 μm respectively. The lateral resolution, defined by the geometric projection of the focused beam onto the sample (x and y axes), was adapted to the size of the image and ranged from $3 \times 3\mu m^2$ to $0.5 \times 0.5\mu m^2$. The integration time, tuned from 100 ms pixel^{-1} and 5 s pixel^{-1}, was determined by both the concentration of the emitting elements and the signal-to-noise ratio of the fluorescence signal.

Ice adjacent to the samples was analyzed by ion chromatography, in order to establish the average concentrations of the main ionic species of the melted ice (Table 1) (Saigne and others, 1987). The concentrations ranged from 0.13 to 938 ng g^{-1}.

3. RESULTS AND DISCUSSION

3.1. Technique validation

Control of the experimental procedure and background estimation

To estimate the contamination introduced by the sample preparation and to test the influence of the Ultralene® film, two XRF spectra (Fig. 2) were taken under the same experimental conditions as for the polar ice samples: one using a sample cell filled with air and the other using an artificial sample (S1), which was also analyzed by ion chromatography (see Table 1). To take account of the variations in the incoming intensity (I_o) during experiments, all the figures presented in this paper show the relative intensity, i.e. the ratio (I/I_o) of the emitted signal (I) to the incoming intensity. The results for both the air-filled cell and S1 (Table 2) are similar for the chloride peak. Since Cl was not detected by ion chromatography of S1, the Ultralene® film, which is very close to the sample surface, is the most likely source of the Cl peak.

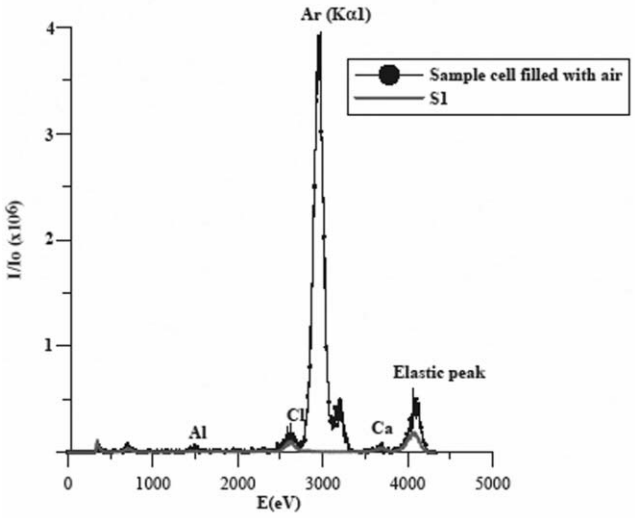

Fig. 2. μXRF spectra from the sample cell filled with air and from the artificial sample (S1). The spectrum from the sample cell filled with air is characterized by a high peak from argon. This result shows the presence of air in the sample cell.

Regarding elements other than Cl (Table 2), the Al peak was lower for S1 than for the cell filled with air. This may be due to the partial absorption of the cell signal by the S1 sample. It was decided that the μXRF signal for an element in S1 would be taken as the background signal. To consider an element as present in polar ice, the μXRF signal should be more than two times higher than the element's signal in S1.

Sample conservation during the experiment

The major risk of transformation of samples is sublimation. Sublimation can be due to a lack of closure of the sample cell in the vacuum chamber. Figure 2 shows the μXRF spectrum for the sample cell filled with air; there is a high peak for argon. Although present as traces in air, Ar has been detected due to its atomic number (18) which explains its good fluorescence response. This Ar peak confirms that the sample cell is airtight.

To check both the stability of the sample and the reproducibility of the technique, an inclusion containing Si

Table 1. Concentrations (ng g^{-1}) measured by ion chromatography for artificial sample (S1), Dome C (DC1) and Vostok samples (V1, V2)

	Ca^{2+}	K^+	Cl^-	MSA	SO_4^{2-}	Si^{2+}	Al^{3+}	Mg^{2+}	Na^+	F^-	NO_3^-	NH_4^+
S1	0.87	0.28	–	–	0.30	–	–	0.13	0.35	0.29	–	0.21
DC1	2.34	1.30	15.35	1.22	80.5	–	–	2.61	20.4	0.70	14.4	–
V1	94.9	5.00	938	–	215	–	–	0.21	798	3.13	1.73	1.71
V2	14.6	9.00	721	–	44.1	–	–	4.51	623	2.33	1.97	0.45

Notes: No visible aggregate in V1 and V2. MSA: methanesulphonate. Dash indicates not detected.

https://doi.org/10.3189/172756505781829340 Published online by Cambridge University Press

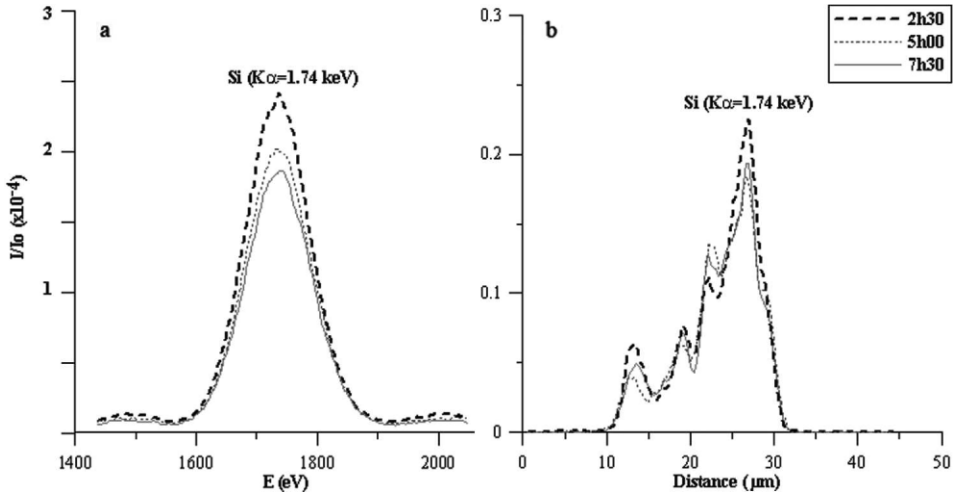

Fig. 3. (a) µXRF spectra (only Si K_α line shown) from an inclusion observed in sample V2 (Vostok at 3572 m) for different radiation exposure times (2.5, 5 and 7.5 hours). (b) Relative-intensity profiles of the Si K_α line along the cross-section of the inclusion. The absence of significant variations confirms the preservation of the sample, even after long exposure times.

in the Vostok sample at 3572 m depth (V2) has been examined three times at 2.5 hour intervals. The µXRF spectra (only Si K_α line relative intensity) and shape of the Si peaks along the cross-section of the inclusion are shown in Figure 3a and b. Whilst the shape of the inclusion is unchanged (Fig. 3b), a slight decrease of I/I_o is observed (Fig. 3a). This suggests a slow evolution of the sample. The decrease is limited to about 20% after >7 hours. This confirms the experiment is non-destructive and can be reproduced.

Several experiments were carried out on the same part of an inclusion containing Cl in the Vostok sample at 3572 m depth (V1). From optical microscopy, this inclusion appears like a spherical grain (2 µm). Table 3 shows the stability of I/I_o for Cl in this inclusion after use of different integration times. This stability means that integration times can be increased (at least by up to 5 s) to improve the sensitivity of the technique without causing elemental repartition. Between each scan, optical microscopy showed that the inclusion was unchanged and that the surface of the sample was not altered by the radiation from the microscope.

3.2. First results

Results from DC1 at 566 m depth

The observation of sample DC1 by optical microscopy shows a homogeneous surface, apart from the grain boundary. The total area mapped by µXRF was $200 \times 188\,\mu m^2$, with a pixel size of 2.6 (x) × 2.6 (y) μm^2, an integration time of 3.3 s and an excitation energy of 4500 eV. Note that the signal includes information from a thickness of about 50 µm below each pixel. The potassium map (Fig. 4) shows a strong concentration of K along the grain boundary. This result is observed under the non-destructive conditions of the technique. This can be explained by the concept that K, which in most cases is in an easily soluble form, should be preferentially found along the grain boundaries or associated with insoluble particles. Other elements, such as Si, Al, S and Ca, were also detected. However, instead of being, like K, highly concentrated in a specific area, they are either concentrated only on a few points or distributed in a homogeneous way throughout the mapped area. As a result, their maps show either a few dark points or a grey area without contrast. This is why, instead of their maps, we show their relative intensity profiles in three selected regions of the map identified as Z1, Z2 and Z3 (Fig. 5).

The I/I_o signals for Si, Al, Ca and K are < 0.04 except from specific spots. For example, Ca is present specifically at points A and B close to the triple junction (Figs 4 and 5) and point C. Except for a very intense point (A in Fig. 4; $I/I_o \sim 16$), the signal for S (Fig. 5; Z2, Z3) is about four times higher than the I/I_o signal for the other elements. The origin of S is likely to be H_2SO_4 throughout the matrix. The intense point may originate from an insoluble particle of $CaSO_4$. Owing to the long integration time of 3.3 s, and in spite of the sensitivity for Si and Al being lower than for Ca, it is noteworthy that Si and Al were detected at points A–C.

Table 2. µXRF results from test samples (artificial ice (S1) and sample cell filled with air)

	Ca	K	Cl	S	Si	Al	Mg	Na	F
Energy (keV)	3.69	3.31	2.62	2.31	1.74	1.48	1.25	1.04	0.67
I/I_o (S1)	3.64	0.36	10.52	2.03	1.23	0.91	0.27	0.15	2.82
I/I_o (sample cell filled with air)	3.20	0.80	15.15	1.59	2.40	3.20	–	–	2.40
Ratio of relative intensity to background	*0.88*	*2.22*	*1.44*	*0.78*	*1.95*	*3.52*	–	–	*0.85*

Notes: The energy (keV) corresponds to the K_α emission line. Relative intensity of signal ($\times 10^{-8}$), I/I_o where I is the signal emitted by the element and I_o the incoming intensity. The ratio of the relative intensity to background was measured on S1. Values lower than 2.0 are not considered significant. Dash indicates not detected.

https://doi.org/10.3189/172756505781829340 Published online by Cambridge University Press

Table 3. Evolution of Cl relative intensity in an aggregate for different integration times

	Integration time s	Relative intensity $\times 10^{-8}$
Scan 1	1	234
Scan 2	0.1	236
Scan 3	5	242

Notes: The relative intensity of Cl in the ice, apart from the aggregate, is 10.5×10^{-8}. An estimate of the standard deviation of the relative intensity (234×10^{-8} to 242×10^{-8}) in this aggregate is $\pm 70 \times 10^{-8}$. Between scans 1 and 2, an optical microscopy observation was made over a 30 s period. Between scans 2 and 3 the same observation was made over 60 s. Both observations showed the grain was unaltered.

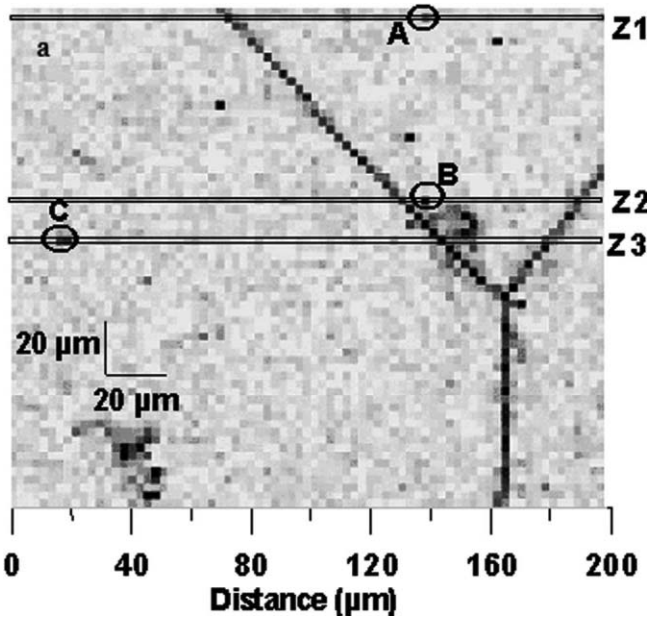

Fig. 4. Map of fluorescence yield of potassium (DC1 sample). Pixel size $2.6 \times 2.6\,\mu m^2$ integration time 3.3 s. Z1 scan refers to the A particle, Z2 to B, Z3 to C. K is clearly found along the grain boundaries (the Y shape on the right of the map).

Results from Vostok samples V1 and V2

The V1 sample (3551 m depth) shows very large crystals (Duval and others, 1998; Jouzel and others, 1999), with some inclusions visible by optical microscopy and a large aggregate visible to the naked eye (Fig. 6a). Such an aggregate, not observed in normal glacier ice, is formed by the concentration and compression of very small particles locally accumulated during the accretion of ice. The gas around the aggregate was initially at ~300 bar, making the aggregate very unstable. To make use of the non-destructive character of the technique, three adjacent elemental maps were drawn. The area of each map was $100 \times 100\,\mu m^2$, with a pixel size of 1 $(x) \times 1$ $(y)\,\mu m^2$ and an integration time of 0.5 s, resulting in 1.5 hours per map. Note that the signal includes information from a thickness of about 50 µm below each pixel.

Figure 6b shows the Ca map distributed as large particles of ~15 µm, with their shapes and spectra being different

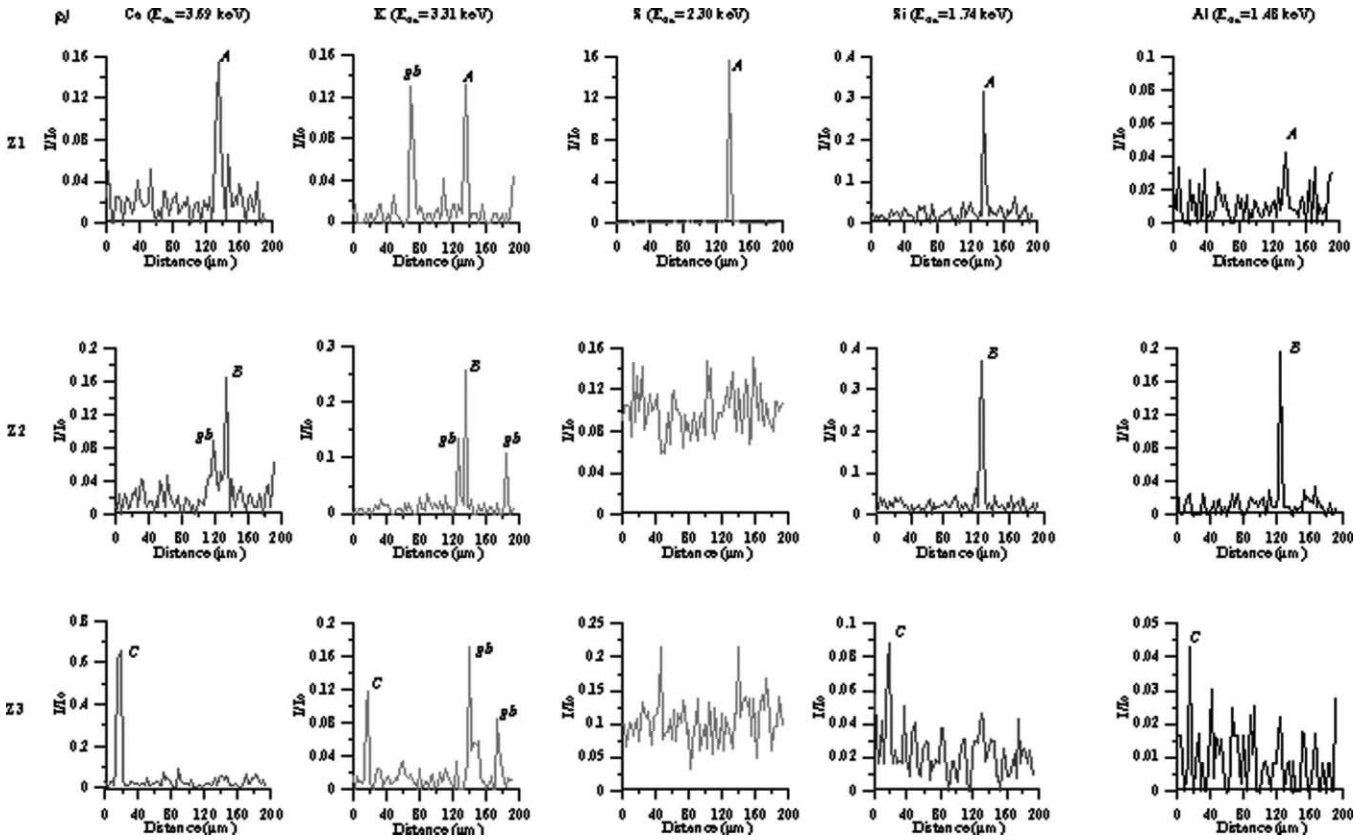

Fig. 5. Relative intensity profiles (Ca, K, S, Si, Al K_α line) along cross-sections Z1, Z2 and Z3 (see Fig. 4; gb indicates the grain boundary). Si and Al are highly concentrated on two specific points (A and B). Si and Al could be within clay particles and associated with Ca (A, B). S is associated with Ca in one highly concentrated spot (A).

https://doi.org/10.3189/172756505781829340 Published online by Cambridge University Press

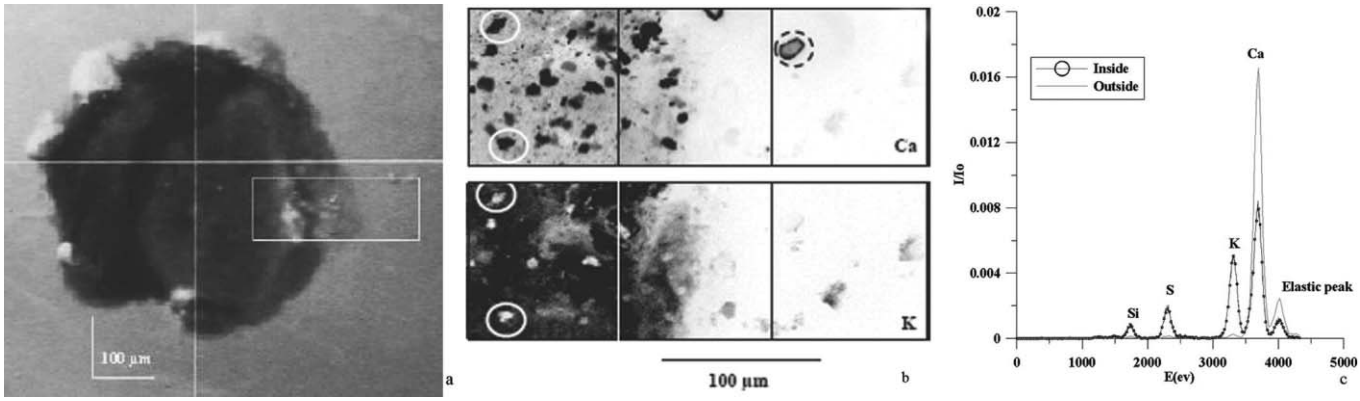

Fig. 6. (a) Aggregate observed on the V1 sample (Vostok at 3551 m). The lighter regions (visible at the periphery) may be gas bubbles, while the dark regions look like the solid part of the aggregate. The rectangular region indicated was analyzed by µXRF. (b) Results of the analysis: maps of Ca and K distributed on the aggregate (image size $300 \times 100\,\mu m^2$; pixel size: $1 \times 1\,\mu m^2$; integration time 0.5 s). Ca is distributed as large particles. Their shapes and compositions are different inside (circles) and outside (dashed circle) the aggregate. Ca seems anticorrelated with K (white circles). (c) µXRF spectra from the upper particles inside and outside the aggregate (circled in (b)).

inside and outside the aggregate (Fig. 6c). Inside the aggregate, Ca appears to be anticorrelated with K (Fig. 6b). Ca predominates outside the aggregate, probably within one $CaCO_3$ inclusion (dashed circle). In case the aggregate might disappear due to its unstable state, several rapid scans (<1.5 hours each) were made to capture the maximum information. S was observed, concentrated at the border and probably associated with Al, although the sensitivity for Al was low. Work is being carried out to confirm and refine these results (de Angelis and others, 2005).

Apart from the one large aggregate, some further inclusions were observed by optical microscopy, and then scanned. The signal intensity (I) for each element as well as its ratio (I/I_o) to the intensity measured on the artificial sample S1 are reported in Table 4. Results for V1 are not significantly different than for S1. As ion chromatography of V1 had shown high concentrations of the species of interest (Table 1), this confirmed that the matrix was pure (de Angelis and others, 2004) and suggests that all impurities were strongly concentrated in inclusions. S was mainly found in the large aggregate, while Cl was in the inclusions in the form of NaCl.

It should be noted that, by assessing the number of inclusions, their volumes and the volume explored in the map, a rough evaluation of the NaCl concentration in the inclusions may be derived from the average concentration measured by ion chromatography.

The V2 sample (3572 m depth) was used to test the potential of the new technique to obtain speciation by selecting the energy of the incident beam according to the oxidation number of the target element. Absorption spectroscopy techniques are based on the measurement of the absorption coefficient of variation by tuning the energy of the probing photons through an absorption edge. This variation is physically related to the excitation cross-section of the core electrons into unoccupied electronic states or into vacuum continua. The spectral features observed close to the absorption edge – referred to as X-ray absorption near-edge structure (XANES) – reflect the molecular environment of a given absorbing atom and provide the basic mechanism for imaging with chemical sensitivity (Stöhr, 1992). Obtaining information on different chemical states within systems having the same elemental composition is possible (Cuif and others, 2003).

An observation was made of a spot showing a particle including Si, Al, P and S (Fig. 7). The size of the image is $50 \times 40\,\mu m^2$, with a pixel size of 0.5 (x) × 0.5 (y), and an integration time of 0.5 s. Note that the signal includes information from a thickness of about 25 µm below each pixel. The size of the particle is $20 \times 13.5\,\mu m^2$. Figure 7a–c,

Table 4. Relative intensities for various elements measured in natural samples

	Ca	K	Cl	S	Si	Al	Mg	Na	F
E (keV)	3.69	3.31	2.62	2.31	1.74	1.48	1.25	1.04	0.67
I/I_o V1 in the ice matrix	4.74	0.37	25.4	2.74	1.05	0.85	0.49	0.24	1.72
Ratio to background	*1.30*	*1.03*	*2.41*	*1.35*	*0.85*	*0.93*	*1.81*	*1.60*	*0.61*
I/I_o V1 aggregate	897	1950	27.9	757	277	45.9	31.0	2.32	5.51
Ratio to background	*246*	*5417*	*2.65*	*373*	*225*	*50.4*	*115*	*15.5*	*1.95*
I/I_o V1 inclusion	1.63	2.45	299	12.9	2.46	0.82	0.82	3.28	3.28
Ratio to background	*0.45*	*6.81*	*28.4*	*6.35*	*2.00*	*0.90*	*3.04*	*21.9*	*1.16*
I/I_o V2 in the ice matrix	4.72	0.26	11.6	0.79	1.57	1.05	–	0.26	1.57
Ratio to background	*1.30*	*0.72*	*1.10*	*0.39*	*1.28*	*1.15*	–	*1.73*	*0.56*

Notes: The energy (keV) corresponds to the K_α emission line. Relative intensity of signal ($\times 10^{-8}$), I/I_o where I is the signal emitted by the element and I_o the incoming intensity. Ratio between the relative intensity and the background as measured on artificial sample (Table 2). Values lower than 2.0 are not considered significant. Dash indicates not detected.

https://doi.org/10.3189/172756505781829340 Published online by Cambridge University Press

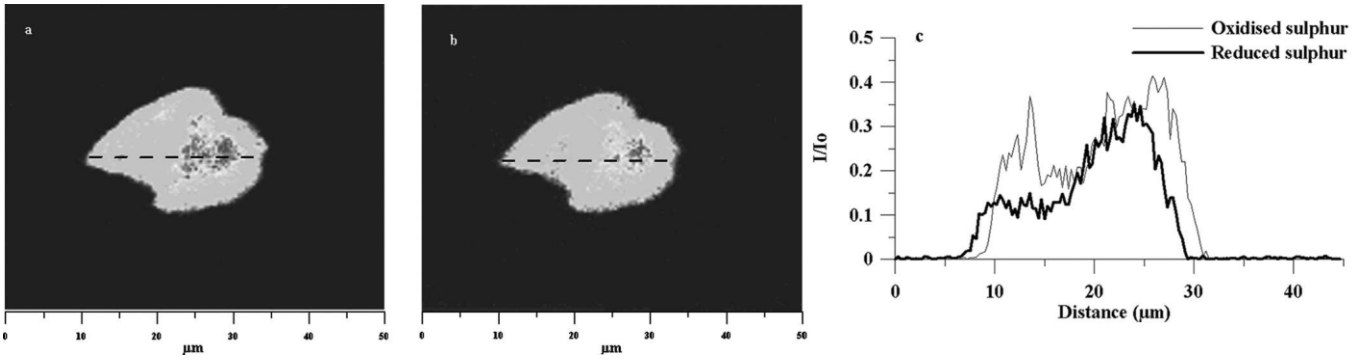

Fig. 7. (a) Map of S (oxidized form) on the inclusion observed in sample V2 (Vostok at 3572 m) using 2.482 keV, image size $50 \times 40\,\mu m^2$, pixel size $0.5 \times 0.5\,\mu m^2$, integration time 0.5 s. (The dashed line indicates the cross-section analyzed in (c).) (b) Map of S (reduced form) on the inclusion observed in sample V2 using 2.473 keV, image size $50 \times 40\,\mu m^2$, pixel size: $0.5 \times 0.5\,\mu m^2$, integration time 0.5 s. (The dashed line indicates the cross-section analyzed in (c).) (c) Relative intensity profiles from the oxidized and reduced forms of sulphur along the cross-section.

respectively, show oxidized sulphur using an excitation energy of 2.482 keV, reduced sulphur using an excitation energy of 2.473 keV, and their different localizations. By supplying cartographies of elements for their different oxidation numbers, the technique yields information that can help to determine the sources of the impurities.

CONCLUSIONS

μXRF analyses of polar ice samples were carried out after adaptations of both equipment and methodology. Results obtained from Dome C and Vostok samples are the first results obtained from the technique. The thermal control system keeps ice samples unchanged during analysis. Integration times can be increased without alteration of samples. Sensitivity can be optimized by increasing integration times, and for a given beam energy the set of identified elements is expanded. For a given time window, optimization results from a trade-off between integration time and resolution. For the selected samples, impurities were not altered by the analyses. As the elements within impurities were kept highly concentrated, they were detectable, although their average concentrations, measured on melted samples by ion chromatography, are far below the detection limit of μXRF.

By selecting integration time, resolution and size of the area to be mapped, analysis times can be shortened to about 1 hour which enables us to scrutinize unstable impurities. Being non-destructive, this μXRF technique makes it possible to reproduce experiments to confirm or refine results.

Beyond the detection of elements within impurities, the technique enables their speciation, which may help with finding the origins of impurities. In conjunction with the technical adaptations, the use of artificial ice samples was included in the analysis process. By measuring background μXRF signals from artificial samples, it was possible to detect artefacts or contamination due to experimental conditions. Combined with the reproducibility of experiments, this brings reliability to the results and to the related forthcoming glaciological interpretations.

ACKNOWLEDGEMENTS

We thank the ESRF for providing the X-ray facilities ME481 and CH1568, and the EPICA and Vostok programmes for ice samples. We thank M. Salomé for assistance on beamline ID21, R. Pieritz for help during the experiment and C. David, T. Weitkamp and E. Di Fabrizio for providing zone plates. We thank S. Nagorski for improving the English. We also thank Centre National de la Recherche Scientifique, France/Institut National des Sciences de l'Univers (CNRS/INSU) (Groupement de Recherche Européen (GDRE) Vostok) for supporting this work.

REFERENCES

Baker, I. and D. Cullen. 2003. SEM/EDS observations of impurities in polar ice: artifacts or not? *J. Glaciol.,* **49**(165), 184–190.

Baker, I., D. Cullen and D. Iliescu. 2003. The microstructure location of impurities in ice. *Can. J. Phys.,* **81**, 1–9.

Barnes, P.R.F., R. Mulvaney, E.W. Wolff and K. Robinson. 2002. A technique for the examination of polar ice using the scanning electron microscope. *J. Microsc.,* **205**(2), 118–124.

Barnes, P.R.F., E. Wolff, D.C. Mallard and H.M. Mader. 2003. SEM studies of the morphology and chemistry of polar ice. *Microsc. Res. Techn.,* **62**, 62–69.

Cuif, J.P., Y. Dauphin, J. Doucet, M. Salome and J. Susini. 2003. XANES mapping of organic sulfate in three scleractinian coral skeletons. *Geochim. Cosmochim. Acta,* **67**(1), 75–83.

Cullen, D. and I. Baker. 2002. Observation of sulfate crystallites in Vostok accretion ice. *Materials Characterization,* **48**(4), 263–269.

de Angelis, M., J.R. Petit, J. Savarino, R. Souchez, and M.H. Thiemens. 2004. Contributions of an ancient evoporitic-type reservoir to subglacial lake Vostok chemistry. *Earth Planet. Sci. Lett.,* **222**(3–4), 751–765.

de Angelis, M., M.C. Morel Fourcade, J.M. Barnola, J. Susini and P. Duval. 2005. Brine microdroplets and solid inclusions in accreted ice from Lake Vostok (East Antarctica). *Geophys. Res. Lett.*, **32**(12), L12501. (10.1029/2005GL022460.)

Di Fabrizio, E. *and 6 others*. 1999. High efficiency multilevel zone plates for keV X-rays. *Nature,* **41**(6756), 895–898.

Duval, P., V. Lipenkov, N.I. Barkov and S. De La Chapelle. 1998. Recrystallization and fabric development in the Vostok ice core. *EOS Trans. AGU,* **79**(45), F152. Fall Meet. Suppl., Abstract.

Fukazawa, H., K. Sugiyama, S. Mae, H. Narita and T. Hondoh. 1998. Acid ions at triple junction of Antarctic ice observed by Raman scattering. *Geophys. Res. Lett.,* **25**(15), 2845–2848.

Iliescu, D., I. Baker, and X. Li. 2003. The effects of sulphuric acid on the creep, recrystallization, and electrical properties of ice. *Can. J. Phys.,* **81**(1–2), 395–400.

https://doi.org/10.3189/172756505781829340 Published online by Cambridge University Press

Jouzel, J. *and 9 others*. 1999. More than 200 m of lake ice above subglacial Lake Vostok, Antarctica. *Science,* **286**(5447), 2138–2141.
Legrand, M. and P. Mayewski. 1997. Glaciochemistry of polar ice cores: a review. *Rev. Geophys.,* **35**(3), 219–243.
Mulvaney, R., E.W. Wolff and K. Oates. 1988. Sulphuric acid at grain boundaries in Antarctic ice. *Nature,* **331**(6153), 247–249.
Saigne, C., S. Kirchner and M. Legrand. 1987. Ion-chromatographic measurements of ammonium, fluoride, acetate, formate, and methanesulphonate ions at very low levels in Antarctic ice. *Anal. Chim. Acta,* **203**(1), 11–21.
Stöhr, M. 1992. *NEXAFS spectroscopy*. Berlin, NEXAFS Spectroscopy.
Susini, J., M. Salome, B. Fayard, R. Ortega and B. Kaulich. 2002. The scanning X-ray microprobe at the ESRF 'X-ray microscopy' beamline. *Surf. Rev. Lett.,* **9**(1), 203–211.
Trickett, Y.L., I. Baker and P.M.S. Pradhan. 2000. The effects of sulphuric acid on the mechanical properties of ice single crystals. *J. Glaciol.,* **46**(153), 239–243.
Wolff, E.W., R. Mulvaney and K. Oates. 1988. The location of impurities in Antarctic ice. *Ann. Glaciol.,* **11**, 194–197.

MS received 6 May 2004 and accepted in revised form 4 February 2005